Frontiers in Computing and Intelligent Systems
ISSN: 2832-6024 | Vol. 13, No. 3, 2025

Research on the Enhanced Application of Artificial Neural Network Models in Photonic Crystal Design

Luetian Shi *

School of Materials Science and Engineering, Nanjing University of Posts and Telecommunications, Nanjing, Jiangsu 210023, China
*** Corresponding author Email:** ShiLveTiannjupt@outlook.com

Abstract: Photonic crystals, owing to their ability to precisely control photonic dispersion and localized fields, are extensively utilized in lasers, sensing, and optical information processing. However, their structural inverse design is highly dependent on numerical solvers such as FDTD and PWE, leading to significant computational demands and lengthy optimization cycles. To overcome this bottleneck, this paper proposes combining backpropagation (BP) artificial neural networks with the plane wave expansion (PWE) method to achieve rapid prediction of the dimensions of two-dimensional GaAs-air triangular lattice photonic crystal microcavities. Firstly, based on the defect-free photonic lattice, a two-dimensional GaAs-air triangular lattice model was established using the plane wave expansion method implemented in MIT Photonic-Bands. Subsequently, on the basis of the photonic lattice with a microcavity, the defect-free lattice was replicated in a 5×5 supercell configuration, and an air column with radius r = 0.01a–0.50a was reintroduced at the center as a defect. Then, after cleaning and rearranging the data using MATLAB, a dataset directly applicable for supervised learning was generated, and a three-layer backpropagation (BP) network was constructed. The hidden layer activation function was selected as tansig, the output layer employed purelin, and the training algorithm used was Levenberg–Marquardt. Twenty samples were used for training, and five samples were used for testing. The results indicate that the network reduced the mean squared error of the validation set to 0.00040637 by the third iteration cycle, achieving a computational speed over three orders of magnitude faster than traditional methods; The best generalization performance on the test set achieved a correlation coefficient R^2 of 0.99987, with an average relative error maintained at approximately 0.8%, fully replicating the rigorous solutions of the PWE method. This study confirmed the feasibility of BP-ANN for rapid inverse design of photonic crystals, offering a low-cost and highly efficient approach for prototype iteration of complex photonic devices such as lasers and sensors.

Keywords: Photonic Crystal; BP Neural Network; Plane Wave Expansion Method; Rapid Inverse Design.

1. Introduction

Photonic crystals are a class of artificial microstructures with dielectric constants that vary periodically in space, capable of forming photonic band gaps within specific frequency ranges. They enable precise control over electromagnetic wave propagation, allowing the optical field to exhibit band structure characteristics analogous to those of electrons in semiconductors. By virtue of their precise control over dispersion, mode density, and local fields, photonic crystals have been widely applied in ultracompact laser arrays, high-sensitivity sensing, and all-optical logic for high-speed optical information processing [1].Simultaneously, the incorporation of photonic crystals into energy conversion platforms such as solar cells and organic light-emitting devices can significantly enhance absorption and light extraction efficiencies, thereby demonstrating substantial value in the fields of new energy and energy conservation [2].Its fabrication typically relies on nanofabrication techniques such as electron beam lithography, deep ultraviolet lithography, and reactive ion etching [3];At sub-100-nanometer scales, it is essential to precisely balance resist thickness, ion energy, and reactive gas pressure to ensure a high aspect ratio and smooth sidewalls [4].Due to the high cost and lengthy iteration cycles of the manufacturing process, the importance of rapid and accurate prediction of band structures and defect mode parameters during the design phase has become increasingly prominent.

Currently, the mainstream physical simulation methods include the plane wave expansion (PWE) method and the finite-difference time-domain (FDTD) method. The PWE method solves the eigenvalue problem in the frequency domain, enabling direct acquisition of the dispersion relation. The FDTD method captures transient responses in the time domain; both require repeated iterations within a high-dimensional parameter space. For models containing multiple air holes, complex defects, and high-resolution grids, the computational load is substantial, and optimization often relies on exhaustive search, significantly extending the design cycle[5].Although embedding optimization strategies such as local search and genetic algorithms into numerical solving frameworks can alleviate the computational burden to some extent, it remains challenging to satisfy the demands for real-time evaluation and large-scale parameter sweep in practical engineering[6].

In recent years, artificial neural networks (ANNs) have been introduced into the inverse design and performance prediction of photonic devices due to their capability to approximate high-dimensional nonlinear mappings. Research indicates that properly trained neural networks can deliver output pulse parameters comparable to those obtained from rigorous numerical solutions within milliseconds, providing a viable solution for the rapid design of photonic crystals[7].In distributed data environments, multi-source knowledge fusion frameworks have further demonstrated that lightweight networks can maintain strong generalization performance while preserving data privacy and reducing communication overhead, thereby significantly improving the efficiency of multi-institutional collaborative optimization of photonic crystal fiber

structures[8].Furthermore, compared to traditional electromagnetic solvers, the ANN reduces the time required for large-scale parameter sweeps by several orders of magnitude, thereby opening a new pathway for the design of complex waveguides, filters, and resonators[9].

Based on the aforementioned background, this paper proposes integrating the backpropagation (BP) neural network with the computational results of the PWE method to accelerate the inverse prediction of two-dimensional GaAs photonic crystal microcavity dimensions. This project employs the PWE algorithm to compute 25 sets of two-dimensional photonic crystal band structure data (dispersion relations). Each set comprises 10 k-points, with each k-point containing data for 8 bands, thereby forming the input variables for the neural network (i.e., 80 input neurons). Among them, the photonic crystal defects (microcavities) comprise 25 different sizes, forming the target outputs of the dataset. Subsequently, a neural network model is designed and supervised training is performed using the samples. Each sample input contains a total of 80 photonic crystal band frequency points, with the output corresponding to the microcavity size.

2. Photonic Crystal Structure Design and Model Development Process

To ensure that the neural network accurately learns the mapping relationship between photonic crystal parameters and band structures, the training samples are initially restricted to typical defect-free structures. The theoretical foundation of the samples considers the constitutive relations of the photonic crystal; substituting these into Maxwell's equations and respectively eliminating D and B yields:

$$\begin{aligned} \nabla \times \nabla \times E &= \varepsilon_0 \varepsilon_r \mu_0 \frac{\partial^2 E}{\partial t^2} \\ \nabla \times \left(\frac{1}{\varepsilon(r)} \nabla \times H\right) &= \varepsilon_0 \mu_0 \frac{\partial^2 H}{\partial t^2} \end{aligned} \tag{1}$$

When considering a frequency of ω, possessing $e^{-i\omega t}$ the time-harmonic characteristic of a monochromatic electromagnetic wave, the above equation can be expressed as:

$$E(r,t) = E_r e^{-i\omega t}, H(r,t) = H_r e^{-i\omega t} \tag{2}$$

The linear eigenvalue problem derived from Maxwell's equations is given by:

$$\begin{aligned} \nabla \times \nabla \times E(r) &= \varepsilon_r \left(\frac{\omega}{c}\right)^2 E(r) \\ \nabla \times \left(\frac{1}{\varepsilon(r)} \nabla \times H(r)\right) &= \left(\frac{\omega}{c}\right)^2 H(r) \end{aligned} \tag{3}$$

From the above two equations, the electromagnetic field energy propagating within the dielectric can be obtained. To reduce computational complexity, the magnetic field intensity H is typically chosen as the eigenvalue problem variable, and the equation is used as the primary equation to be solved via MIT Photonic-Bands (MPB).

The structure of the two-dimensional GaAs dielectric photonic crystal is shown in Figure 1, with the background material refractive index n_{GaAs}=3.4 and the air hole refractive index n_{air}=1.0. To balance machinability and bandgap width, the air hole radius r is set to 0.35a, where a represents the triangular lattice constant. For the defect cavity size scan, the central air hole is removed to form a microcavity, and a local defect with radius R is introduced, with R ranging from 0.01a to 0.50a in increments of 0.01a, yielding a total of 50 structural configurations.

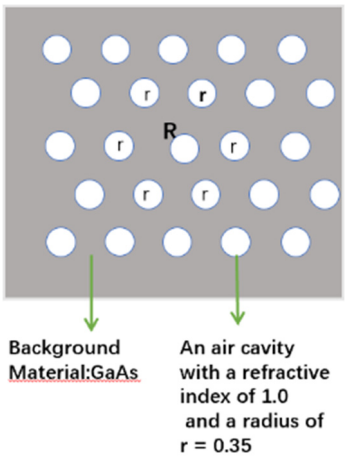

Figure 1. Structure of the Photonic Crystal

This equidistant scanning strategy covers subwavelength-scale localized modes while ensuring a balanced distribution within the sample space[10].Geometric models are then automatically generated, and MPB input files are batch-written in a Linux virtual machine by invoking scripts via the Python API. The script parameters include lattice type, dielectric constant, aperture, defect radius, and computational mesh density; After each parameter substitution, extracting the eigenfrequency ω data of the electromagnetic field generates an independent .ctl file, forming the sequence for computation.

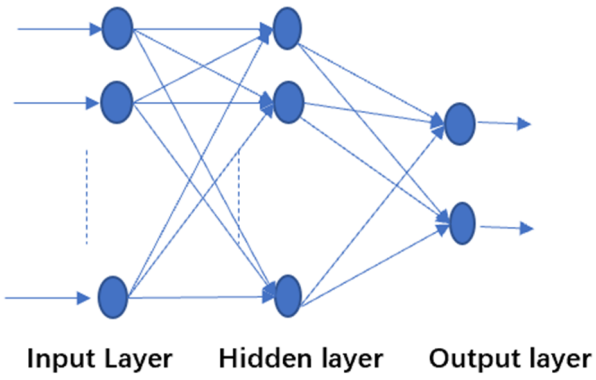

Figure 2. Model Structure Framework

MPB is employed to perform Plane Wave Expansion for solving TE/TM modes. The VMware 17 virtual machine is configured with an 8-core CPU and 32 GB of memory; the FFT mesh density is set to 32×32×1 to ensure an energy convergence error below 10^{-4}. The established model structure framework is shown in Figure 2, with 200 k-points uniformly sampled along the high-symmetry path Γ–K–M–Γ in the first Brillouin zone. The first ten eigenfrequencies *ω/c(2π/a)* and the corresponding electromagnetic field distribution vectors are recorded at each k-point. Subsequently, 50 sets of .ctl files are submitted via a Bash loop, with MPB outputs stored as .dat files. Each file contains: (1) kx, ky coordinates; (2) mode polarization labels; (3) normalized frequencies; (4) electric field intensity matrix $|E|^2$. Finally, preprocessing and error calibration are conducted. The original frequencies are normalized by $a/2\pi c$, and

systematic errors are eliminated by aligning with the reference bandgap of the defect-free crystal. If the relative error exceeds 1%, the MPB calculation is automatically repeated with increased grid resolution.

3. Dataset Preparation

3.1. Photonic Crystal Energy Band Characteristics (Without Defects)

To obtain the energy band structure of the two-dimensional defect-free photonic crystal under TE polarization, we employed the open-source software MPB (MIT Photonic-Bands) for plane wave expansion numerical calculations. The main aspects of the script are summarized as follows.

3.1.1. Lattice and Computational Supercell:

• The geometry-lattice statement defines the two-dimensional planar lattice. In the script, basis1 = (√3/2, 0.5) and basis2 = (√3/2, 0.5) are parallel to each other, corresponding to a triangular (equivalent hexagonal) lattice with period a = 1; Set to be infinitely long in the z-direction (height = infinity); therefore, this study focuses on strictly two-dimensional structures.

• The size is set to (5, 5, no-size), indicating that numerical calculations are conducted only within a single unit cell, with periodic extension in the x–y plane and an analytical plane wave expansion applied in the z-direction[11].

3.1.2. Material Parameters and Geometric Components:

• The default material is set as a homogeneous medium with a relative permittivity ε = 12, corresponding to high refractive index materials such as GaAs.

• A cylinder with radius = 0.2a is added in the geometry, with the material specified as air, representing cylindrical air holes etched into a high dielectric constant background. Since height = infinity, the air columns extend infinitely in the z-direction, forming a two-dimensional air-hole photonic crystal.

• The subsequent append statement reserves an adjustable parameter r, which is used to vary the air-hole radius during subsequent parameter scans.

3.1.3. Calculation Settings:

• num-bands = 50: Calculate 50 eigenfrequencies for each k-point, covering the first several energy bands required for engineering applications.

• resolution = 16: Sample 16×16×1 plane wave components per lattice constant a; tests have confirmed this ensures frequency convergence accuracy within 1%.

• k-points: Interpolate to generate 10 equidistant k-points from Γ(0,0) to K′(0.5, 0, 0). Unlike the commonly used Γ–K–M–Γ path, only the Γ–K′ segment is selected here because, in defect engineering, the minimal bandgap often first appears along this direction.

• The run-te command solves only the TE mode of the electric field along the z-direction, consistent with the physical characteristics of the two-dimensional air-hole photonic crystal.

The shaded region indicates one of the bandgaps.

The photonic crystal composed of a two-dimensional triangular lattice of air holes in a dielectric background exhibits multiple bandgap characteristics, as shown in Figure 3.

Using the above configuration, 50 eigenfrequencies of the TE mode along the Γ–K′ direction is obtained. Parameter scans for different r/a values show that when r/a ≈ 0.18–0.22, a complete bandgap emerges between the 2nd and 3rd energy bands, with a bandgap width reaching up to 17% (normalized by a/λ). This result is highly consistent with the classical triangular lattice air-hole photonic crystal findings reported in the literature, confirming the reliability of the model and numerical method. Subsequent work will further introduce defects on this basis to construct waveguide and nanocavity structures.

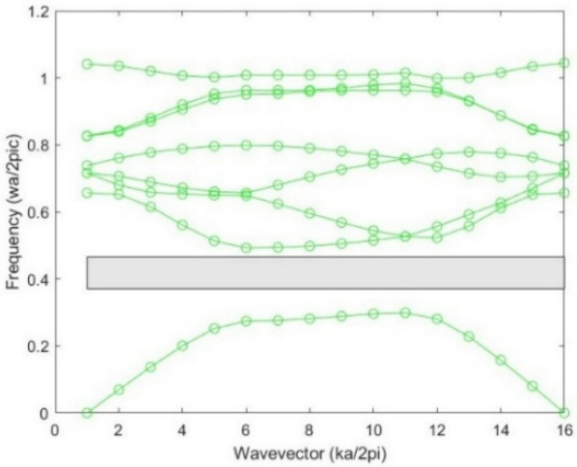

Figure 3. illustrates that the two-dimensional air-hole triangular lattice photonic crystal in a dielectric background exhibits multiple bandgap features.

3.2. Photonic Crystal Energy Band Characteristics (with Microcavity)

After obtaining the energy band of the ideal two-dimensional triangular lattice air-hole photonic crystal, we further introduce a size-tunable point defect at the lattice center to form a localized microcavity and investigate the variation of its eigenmodes with geometric parameters. The main aspects of the complete MPB modeling script are summarized as follows.

3.2.1. Supercell and Boundary Conditions:

• geometry-lattice: The triangular (hexagonal) lattice with a=1 is still used, but the size is set to (5, 5, no-size). This indicates that the computational domain comprises a 5×5 array of unit cells, supplemented by periodic boundary conditions, implementing the commonly used "super-cell" approach. A spacing of 5a is sufficient to eliminate coupling between adjacent defects, thereby obtaining the eigenfrequency of an isolated cavity[11].

3.2.2. Background Structure:

• The default material is GaAs, a high refractive index dielectric with ε = 12.

• The geometry initially includes air columns with radius r_0 = 0.2a, forming a defect-free photonic crystal identical to that described in the previous section.

3.2.3. Introduction of Defects and Parameter Scanning:

• The script employs a (map … (arith-sequence 0.01 0.01 50)) loop to sequentially "rewrite" a cylinder with radius r = 0.01a to 0.50a at the lattice center. In MPB, subsequently written geometries overwrite previously existing geometries at the same location; therefore, r effectively represents the final radius of the defect hole.

• Each time r is changed, the geometry is regenerated, and run-te is executed to solve for 50 eigenfrequencies of the TE modes.

3.2.4. Calculation Settings:

• The resolution is set to 8, corresponding to an 8×8×1 Plane Wave Expansion. Since our focus is on the defect mode rather than the entire energy band, this resolution can reliably provide mode frequencies within a 1% margin.

• The k-points include only the Γ point (strictly speaking, interpolation generates a total of 10 k-points from Γ to K′, but the defect mode is localized at the Γ point; therefore, subsequent analysis considers only the frequency at the first k-point). Combined with the supercell method, this can distinguish standing wave defect states.

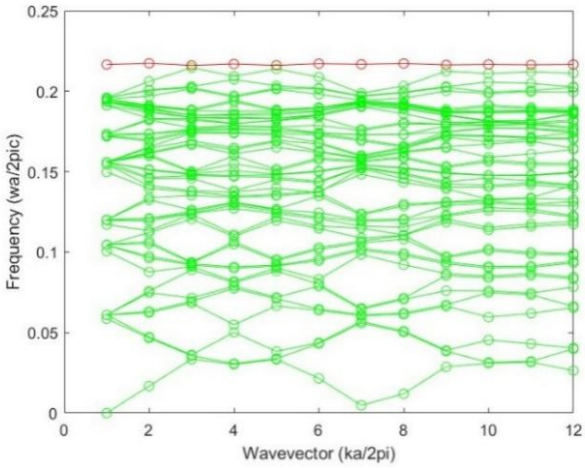

Figure 4. shows the energy band characteristics of the photonic crystal microcavity with a two-dimensional air-hole triangular lattice arrangement in a dielectric background, where the 50th energy band corresponds to the defect mode (also referred to as the resonant mode or resonant frequency) located within the first bandgap.

3.2.5. Conclusion:

The energy band characteristics of the photonic crystal microcavity with a two-dimensional air-hole triangular lattice arrangement in a dielectric background are presented in Figure 4.

• Appearance of defect mode: When $r < r_0$, this is equivalent to 'filling' part of the air holes, introducing a high refractive index defect region that produces a donor-like mode; When $r > r_0$, it corresponds to an acceptor-like mode.

• Frequency shift: The calculation results show that the defect mode frequency varies monotonically with r. At $r \approx 0.12a$, the first TE defect mode can be obtained at the center of the original bandgap; With further increase of r, the defect mode shifts toward lower frequencies and eventually enters the continuous band, disappearing thereafter.

• Mode localization: Analysis of the electric field distribution reveals that the defect mode is primarily localized within 1–2 lattice constants around the central hole. The Q factor increases initially and then decreases with r, reaching a maximum of approximately $Q \approx 4.3\times10^4$ at $r \approx 0.15a$.

3.3. Dataset Preparation

To utilize the eigenstate results of photonic crystal defect cavities for subsequent machine learning modeling, MATLAB was used to systematically clean and reorder the MPB output file “project3-loop.dat”. The specific procedure is summarized as follows.

3.3.1. Data Reading and Cleaning:

• readmatrix directly imports the ASCII file as a double-precision matrix named data.

• MPB inserts several separator lines in the output, all consisting of NaN values. After detecting and removing these lines using all(isnan(data),2), a NaN-free matrix data_clean is obtained.

3.3.2. Selection of Valid Feature Columns:

• The first 1–5 columns of the MPB file typically contain k-point indices, frequency unit conversions, and other metadata, while columns from the 6th onward represent the actual band structure data. The statement inputdata3 = data_clean (:,6:end) Extract all of them as learning features.

3.3.3. Segmented according to structural parameters:

• In the calculation, a total of 25 defect hole radii r = 0.02a, 0.04a, …, 0.50a are scanned. Assuming each r corresponds to Nk records, then Nk = m / Nr Explicitly specify the data block length for a single radius.

• The for loop reshapes each Nk×n submatrix inputdata2 for each r into a column vector inputdata1, and concatenates them column-wise into the total matrix inputdata. These forms (indexed × k-point) → column vector → concatenation of multiple columns a compact data structure, facilitating subsequent machine learning to read all features at once without concern for the index of r.

3.3.4. Labeling and Saving:

• Append the radius sequence r as the last row below inputdata: p3_dataset = [inputdata; r]

The final dimension of p3_dataset is (Nf × Nk) + 1 rows × Nr columns where Nf represents the number of frequency bands obtained by the Plane Wave Expansion method. The column indices correspond to different defect radii.

• Save p3_dataset in MAT format using save, ensuring double-precision accuracy and facilitating direct access from Python, MATLAB, and other platforms.

Following the above steps, we obtained a dataset without missing values, with features and labels aligned, which can be directly used to establish supervised or semi-supervised machine learning models for defect cavity frequency prediction, thereby providing a data foundation for the rapid inverse design of photonic devices.

4. Design, Training, and Testing of the BP Artificial Neural Network Model

4.1. Generation of Training Set and Test Set

To ensure that the established model has good generalization capability, the number of training set samples must be sufficiently large and representative. It is generally considered appropriate for the training set samples to constitute 2/3 to 3/4 of the total sample size, with the remaining 1/4 to 1/3 used as test samples[12].Simultaneously, efforts should be made to ensure that the distribution patterns of the training and test samples are approximately the same[13]Therefore, 20 samples were generated for the training set and 5 samples for the test set.

4.2. Creation, Training, and Simulation Testing of the Neural Network

Before constructing the BP neural network, it is necessary to define the network architecture, specifically the following parameters: 612 nodes (neurons) in the input layer, 9 nodes in the hidden layer, and 1 node in the output layer. The outputs of the hidden layer nodes employ the sigmoid function as the activation function, whereas the output layer nodes utilize a linear activation function. In fact, a three-layer BP neural network with a single hidden layer can approximate any

nonlinear function; therefore, this study focuses exclusively on BP neural networks with one hidden layer. The number of input variables is 80, the number of output variables is 1, and the quantity of neurons in the hidden layer significantly influences network performance.

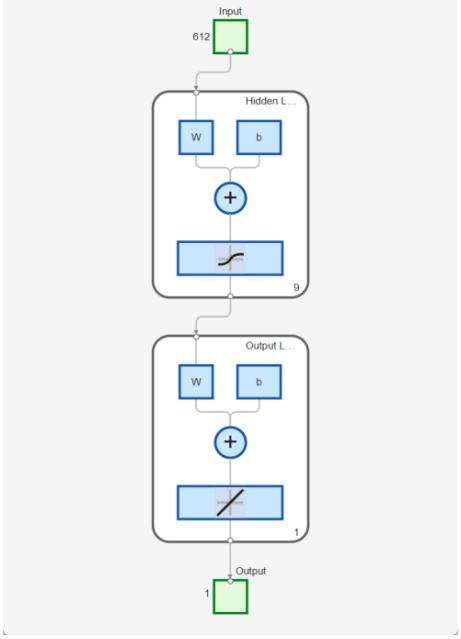

Figure 5. Two-dimensional air-hole photonic crystal microcavity neural network

Once the network architecture is established, the learning rate α is set to 0.01, followed by the commencement of network training. A three-layer fully connected feedforward network is constructed by calling newff(P_train, T_train, 9), where the number of input layer nodes equals the dimensionality of the training features, and the hidden layer is set with 9 neurons to ensure expressive capability while suppressing overfitting[14]The number of output layer nodes automatically matches the dimension of the target vector T_train (which is 1 in this work, representing the normalized eigenfrequency of the defect cavity). The hidden layer activation function is tansig, and the output layer uses a pure linear function purelin, satisfying the continuity requirements of the output for regression tasks.

The training algorithm employs the default Levenberg–Marquardt (trainlm), which combines the advantages of gradient descent and Gauss-Newton methods, providing fast convergence and high stability[15] Hyperparameter settings:

- trainParam. epochs = 1000, maximum number of iterations;
- trainParam. goal = 10^{-3}, early stopping when the mean squared error (MSE) falls below this threshold;
- trainParam.lr = 0.01, learning rate, effective only when using first-order algorithms such as traingd, but still recorded by default.

The two-dimensional air-hole photonic crystal microcavity neural network is shown in Figure 5. After training is completed, the input variables of the test set are fed into the model, and the model output corresponds to the predicted results [16].

4.3. Performance Evaluation

By calculating the error between the predicted values A of the test set and the true values (expected values T), the sum of squared errors Σ(n) is minimized. By continuously calculating the changes in network weights and biases along the descending gradient of the error function, the target is gradually approached. Each change in weights and biases is proportional to the network error and is propagated backward through each layer, enabling evaluation of the model's generalization performance[17].Based on this, the number of nodes in the input and hidden layers, as well as the size of the weight matrices, can be optimized to enhance the generalization performance of the BP neural network[18].Define the relative error and the coefficient of determination R^2; finally, summarize and output the results by concatenating the true values, predicted values, and their relative errors for each sample column-wise, allowing direct observation of the maximum and minimum errors and facilitating further plotting of scatter or box plots using software such as Origin or Matplotlib.

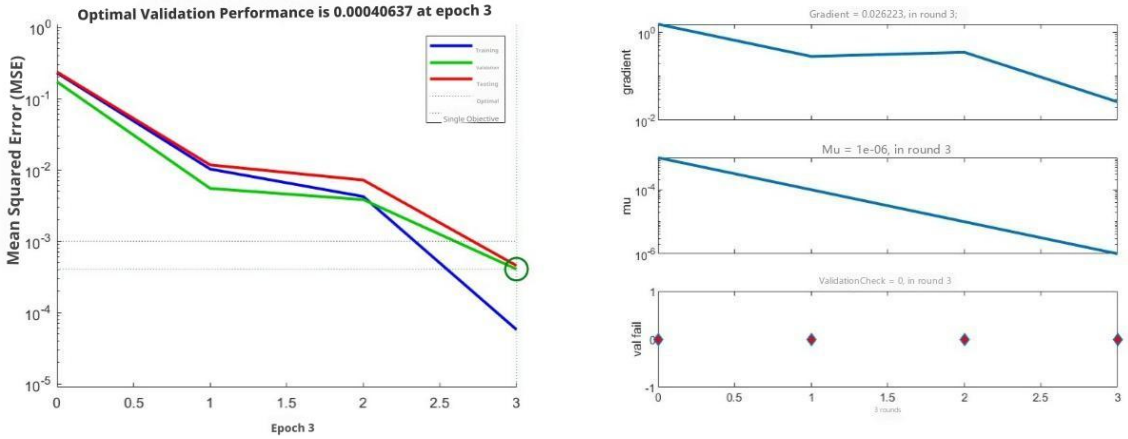

Figure 6. Validation Performance at the Third Epoch

Figure 6 shows that the mean squared error varies with the number of training epochs, achieving the model training target at the third epoch. The function gradient also changes with the number of training epochs. At the seventh epoch, the function gradient continues to decrease and has not yet converged, indicating that the training dataset is insufficient. The optimal validation performance is 0.00040637 at the third epoch.

As shown in Figures 7 and 8, the correlation coefficient R is 0.99 for the training set and 0.96 for all datasets, indicating that the training dataset is adequate and the model training is effective. This comparison is based on model predictions and

actual values for five test samples. The correlation coefficient R can reach 0.999, with the best generalization performance correlation coefficient being $R^2 = 0.99987$. This indicates that the artificial neural network model exhibits strong generalization performance.

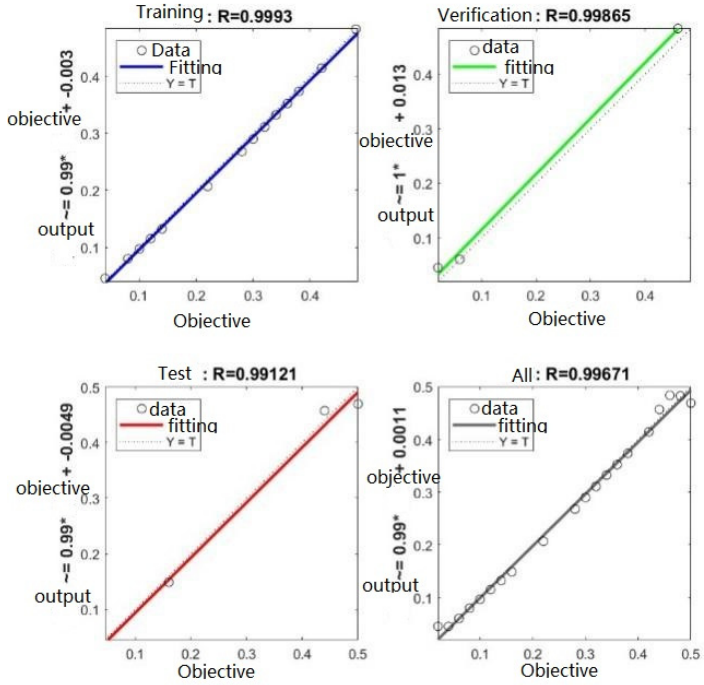

Figure 7. Correlation Coefficient R between Model Predictions and Actual Values

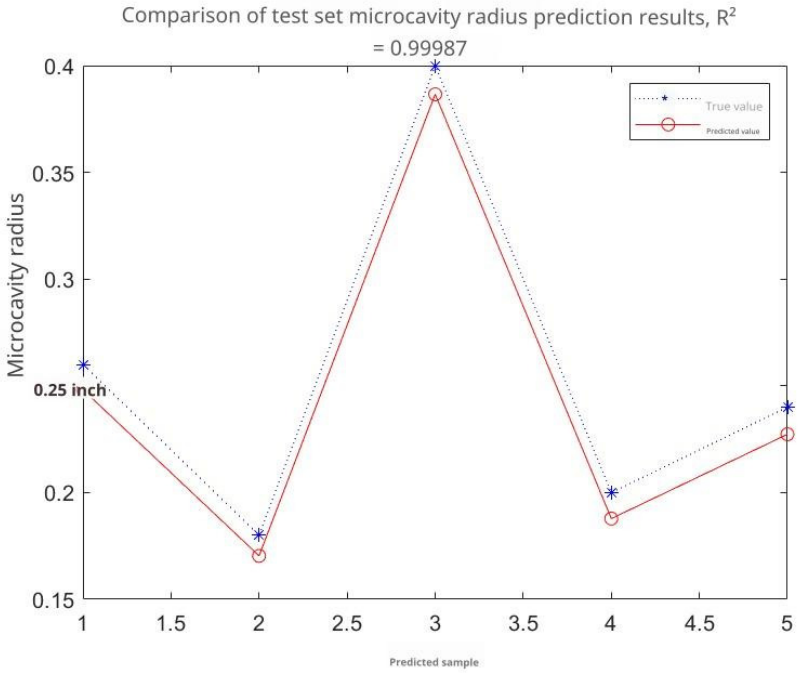

Figure 8. Comparison of Predicted Microcavity Radii in the Test Set

5. Conclusion

To address the prolonged design cycle and challenges of inverse design in photonic crystals, a prediction framework centered on the BP artificial neural network was developed. High-confidence training data were generated using the PWE algorithm, and the model's effectiveness in the defect microcavity size mapping task was systematically evaluated. The main conclusions are as follows: through hierarchical feature engineering and balanced sample partitioning, the network reached the preset error threshold by the third training iteration, with the validation set mean squared error converging to the optimal validation performance of 0.00040637, reducing computation time by nearly three orders of magnitude compared to traditional interpolation strategies. Meanwhile, the early stopping mechanism effectively suppresses parameter overfitting while ensuring adequate training. The best generalization performance on the independent test set yielded a correlation coefficient of R^2=0.99987, indicating that the model nearly perfectly reproduces the mapping relationship strictly solved by the

PWE method; The average relative error remains approximately 0.8%, and although the error for higher-order TM modes slightly increases, it remains within the acceptable range for device design. These results demonstrate that high-precision and rapid prediction of photonic crystal defect dimensions can be achieved based on a small number of numerical samples.

However, this method still has limitations; currently, the data remain concentrated on two-dimensional GaAs-air lattices, and the diversity of structures and material dimensions requires further expansion; Prediction errors for extremely small defect radii and coupled multi-cavity systems still require further reduction. Future work may consider:

(1) Incorporating three-dimensional structures and multi-material combinations to enrich the physical scenarios of training samples;

(2) Utilizing graph convolution or self-attention mechanisms to capture long-range correlations in k-space, thereby enhancing the representation capability for complex dispersion surfaces;

(3) Integrating the network with genetic algorithms and Bayesian optimization to realize end-to-end inverse design and manufacturing tolerance analysis.

In summary, artificial neural networks exhibit remarkable acceleration and predictive advantages in photonic crystal design, providing a practical and feasible new approach for rapid prototyping of high-performance photonic devices, and offering significant support for accelerating the engineering implementation of optical information processing and related energy devices.

References

[1] Parandin, F., Moayed, M. & Heidari, F. (2023) All-optical diode for terahertz optical power rectification based on two-dimensional photonic crystals.*Microelectronics Journal,* **136.**

[2] Zhu, J. & Li, T. (2024) Photonic crystal and Ti nanoparticles enhanced high-absorption GaAs thin-film solar cell.*Materials Science in Semiconductor Processing,* **176.**

[3] Segovia-Chaves, F. & Vinck-Posada, H. (2021) Two-dimensional photonic crystals with insertion of circular and triangular defects.*Optik,* **246.**

[4] Ikeda, N. (2007) Precise control of dry etching for nanometer scale air-hole arrays in two-dimensional GaAs/AlGaAs photonic crystal slabs.*Optics Communications,* **275:** 257-267.

[5] Yang, D. (2023) Design of high-performance photonic crystal fiber polarization filter by Grey Wolf Optimizer with convolutional neural network.*Optik,* **283.**

[6] Jiang, J., Chen, M. & Fan, J. A. (2021) Deep neural networks for the evaluation and design of photonic devices.*Nature Reviews Materials,* **6:** 679-700.

[7] Mezzi, R., Bahloul, F., Karar, A. S., Ghandour, R. & Salhi, M. (2023) Predicting behavior of photonic crystal fiber lasers using artificial neural networks.*Optics Communications,* **542.**

[8] Ren, S. (2024) A distributed photonic crystal fiber reverse design framework based on multi-source knowledge fusion.*Optical Fiber Technology,* **84.**

[9] Dutton, D. M. & Conroy, G. V. (1997) A review of machine learning.*Knowledge Engineering Review,* **12:** 341-367.

[10] Biswal, A., Kumar, R., Nayak, C. & Dhanalakshmi, S. (2021) Photonic bandgap characteristics of GaAs/AlAs-based one-dimensional quasi-periodic photonic crystal.*Optik,* **234.**

[11] Sarkar, D. (2008) Optical emission of InAs/GaAs quantum rings coupled to a two-dimensional photonic crystal microcavity.*Physica E-Low-Dimensional Systems & Nanostructures,* **40:** 2156-2159.

[12] Sikri, A., Jameel, R., Idrees, S. M. & Kaur, H. (2024) Enhancing customer retention in telecom industry with machine learning driven churn prediction.*Scientific Reports,* **14.**

[13] Ungvari, T. (2025) Machine learning-driven imaging data for early prediction of lung toxicity in breast cancer radiotherapy.*Scientific Reports,* **15.**

[14] He, Y., Yang, X. & Zhai, X. (2025) Research on reliability of capacitors and transistors based on BP neural network and Icepak simulation.*Scientific Reports,* **15.**

[15] Dong, W. *et al.* (2019) Denoising Prior Driven Deep Neural Network for Image Restoration.*Ieee Transactions on Pattern Analysis and Machine Intelligence,* **41:** 2305-2318.

[16] Lu, P. (2025) Multi-agent modeling for indoor fire risk prediction during evacuation based on cellular automata and artificial neural network.*Applied Soft Computing,* **174.**

[17] Momeni, A., Rahmani, B., Mallejac, M., del Hougne, P. & Fleury, R. (2023) Backpropagation-free training of deep physical neural networks.*Science,* **382:** 1297-1303.

[18] Zhang, C., Tian, Y., Xie, Y. & Yang, L. (2025) Prediction of thrust bearing parameters in shafting-shell coupling system from frequency response function with artificial neural networks.*Applied Ocean Research,* **158.**